

# Combinatorial Measurements of Crystallization Growth Rate and Morphology in Thin Films of Isotactic Polystyrene

Kathryn L. Beers, Jack F. Douglas, Eric J. Amis, and Alamgir Karim\*

Polymers Division, National Institute of Standards and Technology,  
100 Bureau Drive Stop 8542, Gaithersburg, Maryland 20899-8542

Received October 25, 2002. In Final Form: February 7, 2003

Combinatorial methods are utilized to study the influence of film thickness ( $13 \text{ nm} < h < 120 \text{ nm}$ ) and crystallization temperature ( $131 \text{ }^\circ\text{C} < T_x < 193 \text{ }^\circ\text{C}$ ) on the crystallization of isotactic polystyrene. Films with continuous gradients in film thickness were prepared by flow coating, crystallized on an orthogonal temperature gradient stage, and observed under an optical microscope. Spherulite growth rates were measured as a function of film thickness and temperature, as determined from an optical micrograph library of numerous subregions within the gradient films. We observed that the growth rate had a maximum near  $180 \text{ }^\circ\text{C}$  and varied inversely to film thickness, consistent with the results of Sawamura et al. A transition from hexagonal plate to circular growth was observed with increasing undercooling in the thickness range between 23 and 80 nm. Both hexagonal and disordered branched crystalline morphologies formed in ultrathin regions where the film thickness is less than the radius of gyration.

## Introduction

A new approach in scientific research, using combinatorial methods, has enjoyed demonstrated success in the field of pharmaceuticals and has begun to spread into the area of materials science. Many of these developments have been in the area of polymer science, where adapting the elements of experimental design that have been successful in the areas of drug and catalyst discovery poses unique technical challenges.<sup>1</sup> The complex physical effects governing the morphology of polymeric materials, such as crystallization and the stability of semicrystalline polymer films, can make even the first steps of experimental design, specification and development of a library encompassing a subset of parameter space, daunting.

Recently, the ability to prepare thin films with continuous gradients in composition or film thickness was demonstrated.<sup>2</sup> This technique has been used to investigate polymer dewetting,<sup>3</sup> phase separation in polymer blends,<sup>4</sup> surface pattern formation in symmetric diblock copolymer films<sup>5,6</sup> and photoresist materials and formulations.<sup>7</sup> These investigations have both reproduced previous results and discovered unique insights into well-studied polymer systems, due to the expanded capacity to explore the parameter space governing these phenomena. The method has been shown to be especially valuable in discovering small regions of parameter space where unique phenomena occur.

In the present article, similar methods are used to study crystallization in thin films of isotactic polystyrene, ipS. While the crystal growth of polymers has long been a subject of intense study, only recently has serious attention been focused on the growth rate and morphology of crystals in thin films.<sup>8–10</sup> Previous studies<sup>11–13</sup> of ipS have shown that the growth rates in thin films have a dependence on the crystallization temperature, which does not differ significantly from that of the bulk material.<sup>14–17</sup> Moreover, the crystal morphology was reported to remain unchanged while crystal growth rates,  $G$ , became smaller as the films became thinner, approaching thicknesses commensurate with the radius of gyration and lamellar thicknesses. Of primary interest to the present study is the effect of temperature and film thickness on growth rates and crystal morphology using high-throughput, combinatorial methods.

## Experimental Section<sup>39</sup>

**Materials.** A solution of 90% ipS in toluene (mass fraction, 4.5%) was obtained from Scientific Polymer Products ( $M_r = 6 \times 10^5$ ,  $M_w/M_n = 3.0$ ).<sup>18,19</sup> A sample of the polymer was dried in a

\* Corresponding author. E-mail: alamgir.karim@nist.gov.

(1) Xiang, X.-D.; Sun, X.; Briceno, G.; Lou, Y.; Wang, K.-A.; Chang, H.; Wallace-Freedman, W. G.; Chen, S.-W.; Schultz, P. G. *Science* **1995**, *268*, 1738–1740.

(2) Smith, A. P.; Sehgal, A.; Douglas, J. F.; Karim, A.; Amis, E. J. *Macromol. Rapid Commun.* **2003**, *24*, 131.

(3) Meredith, J. C.; Smith, A. P.; Karim, A.; Amis, E. J. *Macromolecules* **2000**, *33*, 9747.

(4) Meredith, J. C.; Karim, A.; Amis, E. J. *Macromolecules* **2000**, *33*, 5760.

(5) Smith, A. P.; Douglas, J. F.; Meredith, J. C.; Amis, E. J.; Karim, A. *J. Polym. Sci., Part B: Polym. Phys.* **2001**, *39*, 2141.

(6) Smith, A. P.; Douglas, J. F.; Meredith, J. C.; Amis, E. J.; Karim, A. *Phys. Rev. Lett.* **2001**, *87*, 15503-1.

(7) Lenhart, J. L.; Jones, R. L.; Lin, E. K.; Soles, C. L.; Wu, W.-I.; Goldfarb, D. L.; Angelopoulos, M. *J. Vac. Sci. Technol., B*, in press.

(8) Lovinger, A. J.; Cais, R. E. *Macromolecules* **1984**, *17*, 1939.

(9) Sakai, Y.; Imai, M.; Kaji, K.; Tsuji, M. *J. Cryst. Growth* **1999**, *203*, 244.

(10) Reiter, G.; Sommer, J.-U. *J. Chem. Phys.* **2000**, *112*, 4376.

(11) Izumi, K.; Ping, G.; Hashimoto, M.; Toda, A.; Miyaji, H.; Miyamoto, Y.; Nakagawa, Y. *Crystal Growth of Polymers in Thin Films*; Nishinaga, T., Nishioka, K., Harada, J., Sasaki, A., Takei, H., Eds.; Elsevier Science: Amsterdam, 1997; p 337.

(12) Sawamura, S.; Miyaji, H.; Izumi, K.; Sutton, S. I.; Miyamoto, Y. *J. Phys. Soc. Jpn.* **1998**, *67*, 3338.

(13) Taguchi, K.; Miyaji, H.; Izumi, K.; Hoshino, A.; Miyamoto, Y.; Kokawa, R. *Polymer* **2001**, *42*, 7443.

(14) Boon, J.; Krevelen, D. W. V. *J. Polym. Sci., Part A-2* **1968**, *6*, 1791.

(15) Edwards, B. C.; Phillips, P. J. *Polymer* **1974**, *15*, 351.

(16) Hay, J. N. *J. Polym. Sci., Part A: Polym. Chem.* **1965**, *3*, 433.

(17) Suzuki, T.; Kovacs, A. J. *Polym. J.* **1970**, *1*, 82.

(18) This commercial sample of polystyrene was considered commensurate with samples used in refs 11–14 and 25 in molecular weight, polydispersity, and tacticity. Only partial comparison could be made to refs 18 and 27–29 because not all of these data were reported.

(19) According to ISO 31-8, the term “molecular weight” has been replaced by “relative molecular mass,”  $M_r$ . The number-average molecular mass is given by  $M_n$ .

vacuum oven at 110 °C for 48 h, and the observed melt temperature,  $T_m$ , was determined to be 218 °C with a standard uncertainty of 1 °C using a Perkin-Elmer DSC 7 at a scan rate of 5 °C/min for heating and cooling. The original solution was diluted with reagent grade toluene and filtered through a 0.2  $\mu\text{m}$  poly(tetrafluoroethylene) syringe filter before use.

**Library Preparation.** Silicon wafers (Polishing Corp. of America) were cleaved to the desired size and cleaned with soap and water, then heated in  $\text{H}_2\text{SO}_4/\text{H}_2\text{O}_2$  or exposed to UV/ozone to generate an oxide layer, and finally, etched in buffered hydrofluoric acid etch to leave an exposed, hydrophobic Si-H layer. Each wafer was immediately fixed to a robotic stage, and a 30 mm knife-edge was lowered to 200  $\mu\text{m}$  above the surface at a 5° angle. An aliquot (50  $\mu\text{L}$ ) of the ipS solution was deposited by syringe under the knife-edge, and the stage was immediately accelerated under the knife-edge to spread the solution.<sup>4</sup> The solvent evaporated quickly, leaving a thin gradient film that had a local thickness proportional to the instantaneous stage velocity. This procedure is typically referred to as "flow-coating." The range of thickness achieved depends on the viscosity of the solution as well as the velocity of the stage. Each set of experiments consisted of three overlapping gradient films with ranges of thickness between 12 and 120 nm prepared from solutions having mass fractions of 1.0% and 1.5% ipS, respectively (film A, 12 nm <  $h$  < 54 nm; film B, 42 nm <  $h$  < 80 nm; film C, 57 nm <  $h$  < 120 nm).

Film thickness,  $h$ , was measured using an UV-vis reflectance interferometer with a 0.5 mm spot-size mounted over two orthogonal robotic stages (Daedal) such that a two-dimensional array of points was obtained, spaced from 1 to 2 mm apart (see Supporting Information). The standard uncertainty in all measurements of  $h$  was 4%, determined from comparison with atomic force microscopy (AFM) scratch tests. The films were dried overnight in a vacuum oven at 100 °C, heated above the melt temperature in the same oven at 250 °C for 3 min, and quenched to room temperature. The oven temperatures were held constant to within 3 °C. No change in the gradient of film thickness was observed upon repeating the interferometry measurements. In the case of thicker films ( $h > 50$  nm), surface roughness induced by rapid removal of residual solvent was observed upon drying at elevated temperatures.<sup>20</sup> Alternatively, these samples were dried at room temperature under a vacuum for up to several months before melting in order to remove all of the solvent without disturbing the surface of the film.

**Crystallization Measurements.** A Nikon Optiphot-2 microscope was mounted with two orthogonal robotic stages (Newport Corp.) and a preheated gradient temperature stage.<sup>3,5</sup> At the end of each cycle, the stages returned to the start position to within  $\pm 0.5 \mu\text{m}$ . A Kodak Megaplug ES 1.0 CCD camera (1024  $\times$  1024, 8-bit pixels) was used to obtain multiple arrays of optical reflection images. In a typical experiment, an 8  $\times$  8 array of 1000 $\times$  images were obtained at spacings of 2.86 mm along the temperature axis (roughly 10 °C intervals), with  $\Delta h$  between 2 and 10 nm and  $\Delta t = 15$ –30 min, generating a library of approximately 900 images, each representing a point ( $T_x$ ,  $h$ ,  $t$ ) in parameter space. The shallow gradient in temperature ( $dT_x = 0.4$  °C) and height ( $dh = 0.3$  nm) across each image was considered negligible due to the high magnification of the images.

The minimum time interval between samples for a given thickness and temperature is determined by the time required to translate to each position, focus, and capture images and the number of data points (i.e., images) in the array. Using the optical microscope, a minimum time interval of 10 min between data points for an 80-point array was obtained. This is an inherent limitation of optical microscopy, due to the time required to focus at high magnification.

The spherulite size was measured using custom graphics software (NIH ImageJ), and each value reported is an average of between 10 and 30 structures at each point ( $T_x$ ,  $h$ ,  $t$ ). Radius values ranged in size from 5 to 100  $\mu\text{m}$ . The standard uncertainty in each radius value was considered as two standard deviations from the average, typically  $\pm 3 \mu\text{m}$ . Tapping mode AFM using a Digital Instruments Dimension 3100 Nanoscope III and silicon

cantilevers with a spring constant of 30 N/m was used to further investigate the crystal morphologies after the film had been quenched to room temperature. AFM was also used to perform control measurements of film thickness and spherulite radius.

**Temperature Calibration.** The temperature of the aluminum stage was regulated by two embedded thermocouples spaced 4.0 cm apart. Calibration of the temperature at the silicon-air interface of the wafer was carried out using an array of 0.076 mm diameter thermocouples arranged in contact with the silicon surface and held with a thin layer of Arctic Silver thermal compound. A surface plot of the data is also available in the Supporting Information.

Slight deviations were observed between temperatures measured at the air-silicon interface of the silicon wafer and those expected based on the embedded thermocouples. At the lower end of the temperature gradient, differences in the thermal conductivity of the aluminum stage (2.4 W/cm K at 300 K)<sup>21</sup> relative to the silicon wafer (1.5 W/cm K at 300 K)<sup>21</sup> can account for the slower heat loss in the silicon wafer at equilibrium. The slope of the gradient is linear and close to the gradient within the stage between 140 and 180 °C. As temperatures rise above 180 °C, the surface becomes cooler than the stage. This is attributed to convective airflow above the film surface and radiative heat loss. While these deviations are small, they lead to measurable differences in the growth rates at high and low temperatures. Therefore, temperatures are reported relative to these surface measurements rather than the embedded thermocouple readings.

The ipS film was placed with the thickness gradient orthogonal to the temperature gradient such that the temperature of the film spanned 130–200 °C according to the embedded thermocouple measurements. The temperature,  $T_x$ , of the film was later corrected using the data according to  $T_x = 202.1 - 14.1x - 9.1x^2 + 1.5x^3$ , where  $x$  is the distance from the embedded thermocouple at the hot end of the stage, yielding a standard deviation in measured  $T_x$  of 2 °C.

## Results and Discussion

Discrete images illustrating data points for  $T_x$  and  $h$  across a film at a fixed time,  $t = 65$  min (selected from a 9  $\times$  9 array), are shown in Figure 1. This subset represents the range of parameter space that can be spanned on one film. The size and shape of the semicrystalline superstructures in each image illustrate the qualitative differences in morphologies and rates that can be covered using high-throughput methods.

Crystallization growth rates,  $G$ , are calculated from typical optical micrographs shown in Figure 2 for a fixed ( $T_x$ ,  $h$ ) combination at varying time,  $t$ . Because the crystallization of ipS is comparatively slow, it is possible to study the rate of crystallization over a wide range of temperatures, from just below the equilibrium melting temperature,  $T_m$ , to the glass transition temperature,  $T_g$ , at 100 °C. The maximum radius,  $r$ , is plotted as a function of  $t$  as shown in Figure 3 for a range of temperatures and for values of  $h$  between 45 and 50 nm. As the melt-spherulite interfaces approach one another, the area of unincorporated melt is reduced and  $G$  decreases. However, unimpinged interfaces continue to grow at the same rate. Only the linear portion of the growth curve was used to obtain a slope corresponding to  $G$  using linear regression analysis (see figure caption).

As found previously,<sup>11,14–17,22–24</sup> a maximum in  $G$  appears at intermediate temperatures over a wide temper-

(21) Lide, D. R. *CRC Handbook of Chemistry and Physics*, 72nd ed.; CRC Press: Boca Raton, FL, 1991.

(22) Mandelkern, L.; Quinn, F. A.; Flory, P. J. *J. Appl. Phys.* **1954**, *25*, 830.

(23) Kenyon, A. S.; Gross, R. C.; Wurstner, A. L. *J. Polym. Sci.* **1959**, *40*, 159.

(24) Morel, D.; Grubb, D. T. *Polymer* **1984**, *25*, 417.

(20) Strawhecker, K. E.; Kumar, S. K.; Douglas, J. F.; Karim, A. *Macromolecules* **2001**, *34*, 4669.

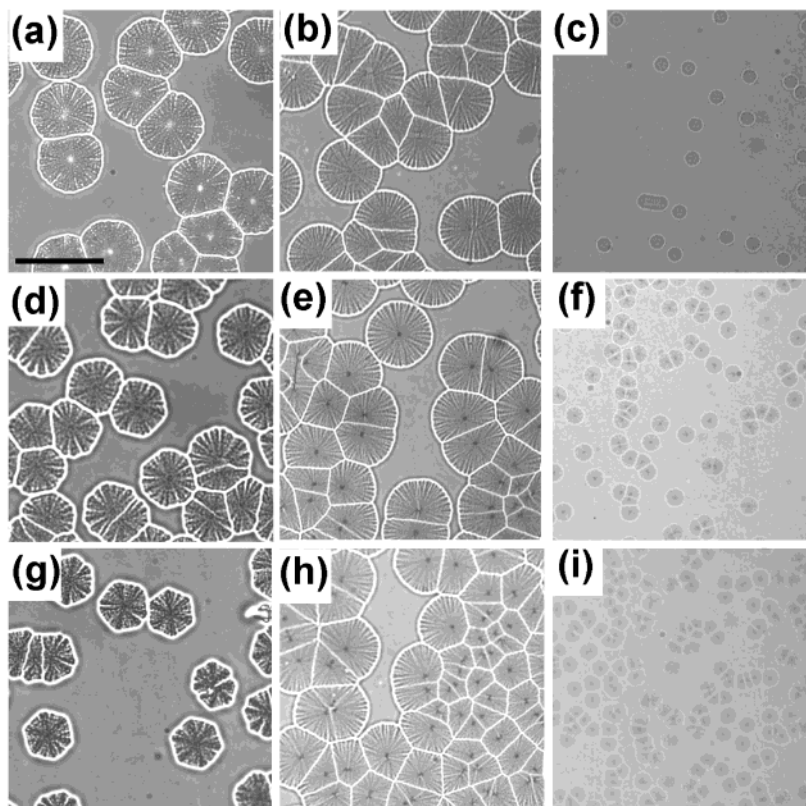


**Figure 1.** Selected images from an image library, illustrating the combinatorial method. The images were taken from an array captured at time  $t = 65$  min and correspond to the following temperatures and film thicknesses, ( $T_x, h$ ): (a) (193 °C, 75 nm), (b) (178 °C, 76 nm), (c) (140 °C, 81 nm), (d) (193 °C, 61 nm), (e) (178 °C, 65 nm), (f) (140 °C, 60 nm), (g) (193 °C, 55 nm), (h) (178 °C, 59 nm), and (i) (140 °C, 52 nm). The scale bar is 50  $\mu\text{m}$ .

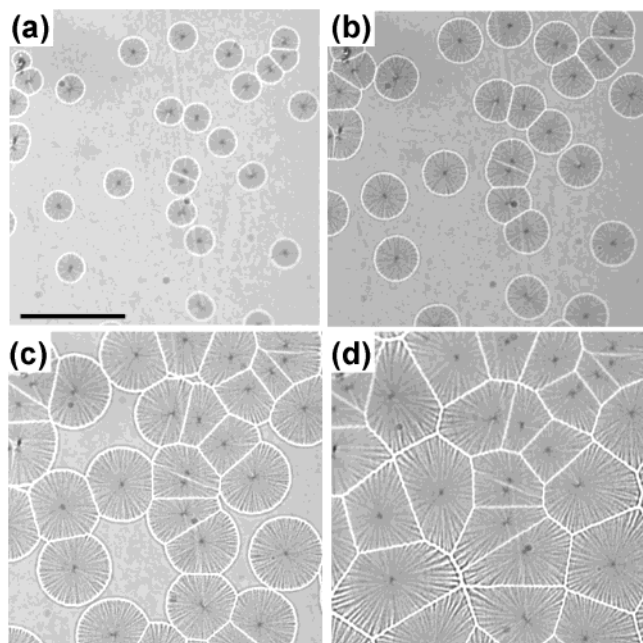


**Figure 2.** Optical microscope images of ipS crystallization kinetics at  $T_x = 169$  °C,  $h = 60$  nm: (a)  $t = 31$  min, (b)  $t = 46$  min, (c)  $t = 81$  min, and (d)  $t = 256$  min. The scale bar is 50  $\mu\text{m}$ .

ature range. This is generally attributed to the competition between the decreased rate of crystallization due to the decreased rate of molecular diffusion upon undercooling and the increase of the rate of secondary nucleation with undercooling.<sup>25,26</sup> The temperature dependence of  $G$  obtained from high-throughput measurements is plotted

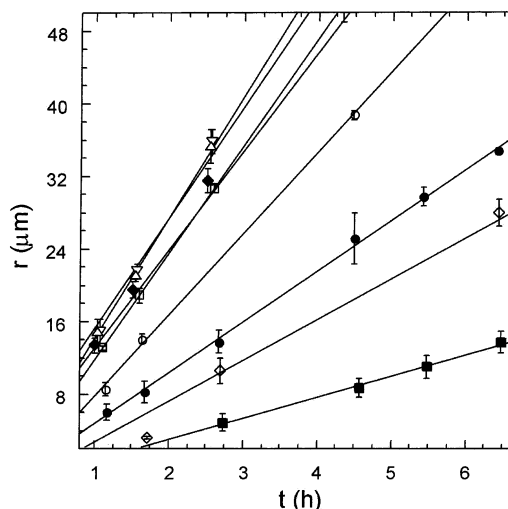


**Figure 3.** The spherulitic radius of semicrystalline ipS plotted as a function of time for a range of temperatures,  $T_x$ , between 131 and 193 °C. Error bars reflect two standard deviations in the average radius measurements. Lines are generated from linear regression analysis to determine slopes ( $G$  in Figures 6 and 8).  $T_x = 131$  °C (■), 140 °C (◇), 150 °C (●), 160 °C (○), 170 °C (□), 178 °C (▽), 186 °C (△), and 193 °C (◆).

in Figure 4, along with data from other references for comparison. All other references in the literature use films of fixed and uniform thickness held at constant temperature. Good agreement is observed between the two methods. While it would be useful in understanding

(25) Brandup, J.; Immergut, E. H.; Grulke, E. A. *Polymer Handbook*, 4th ed.; Wiley-Interscience: New York, 1999.

(26) Magill, J. H. *J. Mater. Sci.* **2001**, *36*, 3143.

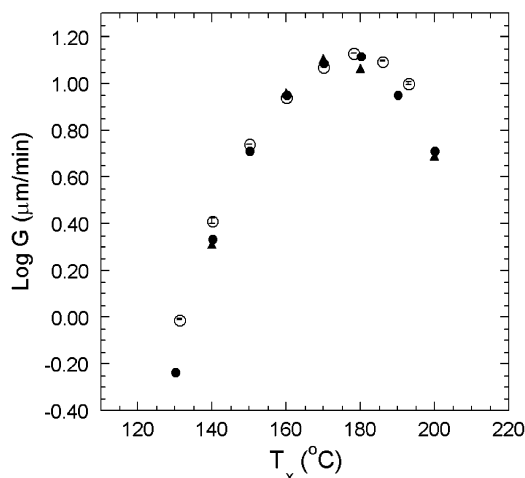


**Figure 4.** The semilogarithmic plot of growth rate,  $G$ , as a function of temperature. A representative sample of data obtained from high-throughput measurements at  $h = 55$  nm (○) are compared with literature values found in refs 13 (●) and 22 (▲). The error bars reflect two standard deviations in the determination of  $G$  and are smaller than the symbols used.

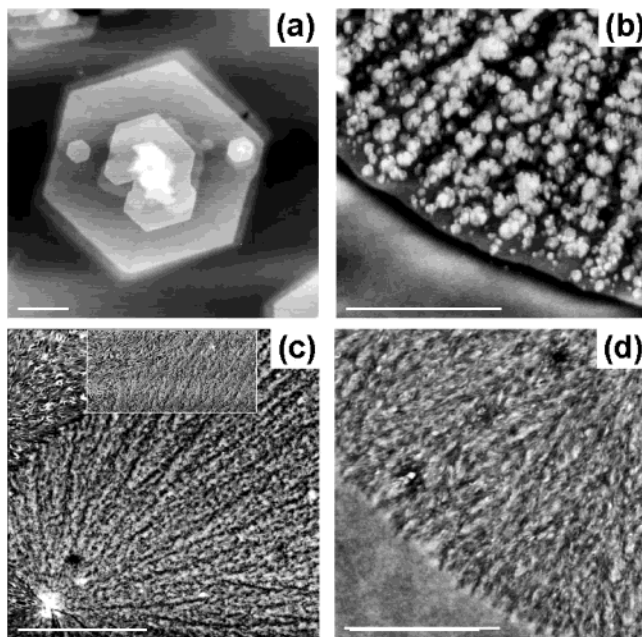


**Figure 5.** AFM height images of ipS crystals grown in thicker regions of the films ( $h > 30$  nm) for 5 h at (a)  $T_x = 202$  °C, (b)  $T_x = 169$  °C, (c)  $T_x = 150$  °C, and (d)  $T_x = 131$  °C. The scale bars are 5  $\mu\text{m}$ . The inset in (C) is a phase image.

crystallization behavior in thin films to look at the trends in  $G_{\text{max}}$  with decreasing  $h$ , only slight deviation from this value was seen for  $h > 22$  nm and the weak contrast of the structures formed below this value prevented measurements by optical microscopy.

Using AFM to observe the crystal morphologies of ipS crystallized at different temperatures also yielded results validating this experimental methodology with measurements reported in the literature.<sup>11</sup> When crystallized at 202 °C, ipS semicrystalline superstructures grow as flat hexagonal crystals. These structures grow with a terraced structure from both the nucleus and other points in the plates resulting from screw dislocations (Figure 5a). When the  $T_x$  drops in the range of 193–170 °C, these dislocations become more numerous, the edges of the semicrystalline structures become increasingly rounded, and the hex-

agonal order radiating from the nucleation sites becomes obscured by dense overgrowth (Figure 5b,c). This secondary nucleation is eventually responsible for the transition from the hexagonal crystal to disordered branched morphology.

At 160 °C, the crystallization patterns have a circular shape at large scales. AFM images captured from regions of the film crystallized at 160 and 150 °C (Figure 5d,e, respectively) show that the terraced structures disappear and randomly branched patterns dominate within the two types of circular growth. The inset in Figure 5c is phase data for an overlapping subregion of the image and shows more clearly the disappearance of terraced growth and existence of branching lamellae. Above a 30 nm thickness, there was no observable dependence of these structures on  $h$ , although some  $h$  dependence has been reported recently for these types of structures in polyethylene in thicker films than those included in the present study.<sup>27</sup> As the temperature drops further to 140 °C or less, only the disordered crystallization structures were observed (Figure 5f).

Previous observations indicate that spherulites are polycrystalline structures resulting from secondary nucleation in the course of crystal growth. Keith and Padden<sup>28–30</sup> have argued that heterogeneous nucleation caused by impurities, including chain defects, is prevalent in spherulite formation. This view was based on reports of spherulite formation in impure small-molecule fluids. Spherulite formation has also been observed, however, in high-purity small-molecule fluids, and this has led Magill and Plazek to suggest that spherulite formation is associated with the low diffusivity (or high viscosity) of highly supercooled liquids.<sup>26,31–33</sup> Preliminary phase field simulations of crystallization in small-molecule liquids suggest that homogeneous secondary nucleation can lead to spherulite formation, so that impurities or defects are not required.<sup>34–36</sup> These simulations also indicate that heterogeneous nucleation by impurities can lead to increasing disorder in the crystallization morphology and a transition from regular dendritic structure to disordered polycrystalline structures.<sup>37</sup> Thus, we suspect the transition from symmetric (hexagonal symmetry) to disordered branched dendritic growth to arise from a combination of homogeneous and heterogeneous nucleation effects, with possible secondary effects associated with non-Newtonian behavior prevalent in supercooled fluids.<sup>32,33</sup>

The bright ring around the outer circumference of the structures in the optical images results from a dip in the film thickness, as indicated by AFM. The width of this ring of depleted film around the crystal structures decreased with crystallization temperature but showed little dependence on  $h$  below 100 nm until the film dropped below 30 nm thick. Both morphological and rate changes were observed as the film became thinner. Although the

(27) Mellbring, O.; Oiseth, S. K.; Krozer, A.; Lausmaa, J.; Hjertberg, T. *Macromolecules* **2001**, *34*, 7496.

(28) Keith, H. D. *J. Polym. Sci., Part B: Polym. Phys.* **1964**, *2*, 4339.

(29) Keith, H. D.; Padden, F. J. *J. Appl. Phys.* **1964**, *35*, 1270.

(30) Keith, H. D.; Padden, F. J. *J. Appl. Phys.* **1964**, *35*, 1286.

(31) Magill, J. H.; Plazek, D. J. *J. Chem. Phys.* **1967**, *46*, 3757.

(32) Simmons, J. H.; Mohr, R. K.; Montrose, C. J. *J. Appl. Phys.* **1982**, *53*, 4075.

(33) Simmons, J. H.; Ochoa, R.; Simmons, K. D.; Mills, J. J. *J. Non-Cryst. Solids* **1988**, *105*, 313.

(34) Gránásy, L.; Börzsönyi, T.; Pusztai, T. *Proceedings of the International Workshop and Seminar on Computational Physics of Transport and Interface Dynamics*, Dresden, 2002.

(35) Gránásy, L.; Iglói, F. *J. Chem. Phys.* **1997**, *107*, 3634.

(36) Gránásy, L.; Börzsönyi, T.; Pusztai, T. *Phys. Rev. Lett.* **2002**, *88*, 206105-1.

(37) Gránásy, L.; Pusztai, T.; Warren, J. A.; Douglas, J. F.; Börzsönyi, T.; Ferreira, V. *Nat. Mater.* **2003**, *2*, 92.

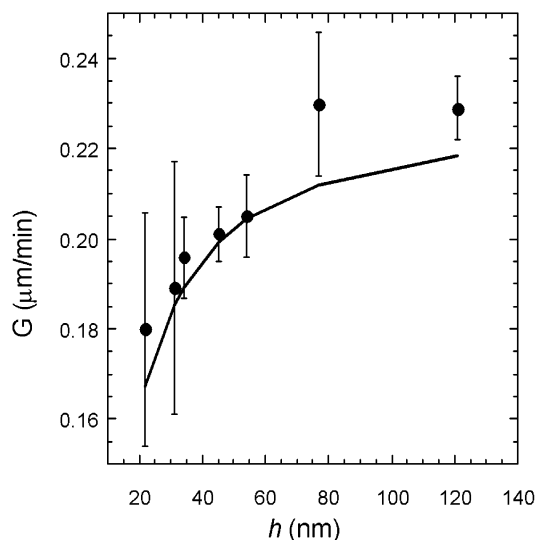


**Figure 6.** The film thickness dependence of  $G$  at  $T_x = 169$  °C. The symbols are data obtained from gradient films. The error bars reflect two standard deviations in the determination of  $G$ . The line is the result of eq 1 in ref 11.

reduced resolution of optical reflection in regions of the films approaching  $h = 20$  nm leads to increases in the uncertainty associated with measuring these rates, a significant decrease in  $G$  with decreasing  $h$  clearly occurs. The data are plotted in Figure 6 along with the curve based on an empirical expression described by Sawamura et al.<sup>12</sup> for multiple uniform thickness films, showing that similar results are obtained by both traditional and high-throughput methods.

Above  $h = 80$  nm, growth rates measured via the high throughput method are higher than expected. This deviation is tentatively attributed to the difficulty in removing solvent from the films in these regions without deforming the surface of the film. In these regions of the films, the temperature at which  $G$  reaches a maximum was also shifted to lower  $T$  due to solvent plasticizing the film and the associated  $T_g$  suppression. The presence of solvent was confirmed by drying amorphous films under a vacuum at elevated temperatures and observing the surface roughness induced by solvent evaporation in the AFM images. In most of the other studies referenced, residual solvent is not an issue because films were prepared by melt pressing.

In the thinnest regions of the films, where  $h$  drops below the radius of gyration of the ipS molecules ( $R_g = 22$  nm), the semicrystalline morphology is observed to change substantially.<sup>13</sup> While it is not clear that these morphological transitions relate directly to molecular mass, it should be kept in mind that this is a commercial polymer sample and it contains a broad distribution of molecular mass. Although it is common to use such a sample in this type of study, as  $h$  drops significantly below  $R_g$ , the influence of shorter chains in the sample may become more significant. It was not considered a factor, however, in the interpretation of our results.

In Figure 7, AFM images taken at different points on the film along the 193 °C isotherm illustrate this transition. At  $h = 24$  nm (Figure 7a), typical hexagonal crystals are formed, while for  $h = 19$  nm (Figure 7b), transition structures between the hexagonal plates and symmetrical dendrite morphologies are observed. At  $h = 15$  nm, the difference in growth rate between the main arms and side branches is clear and overgrowth is almost nonexistent in the dendritic structure. Results showing the growth of

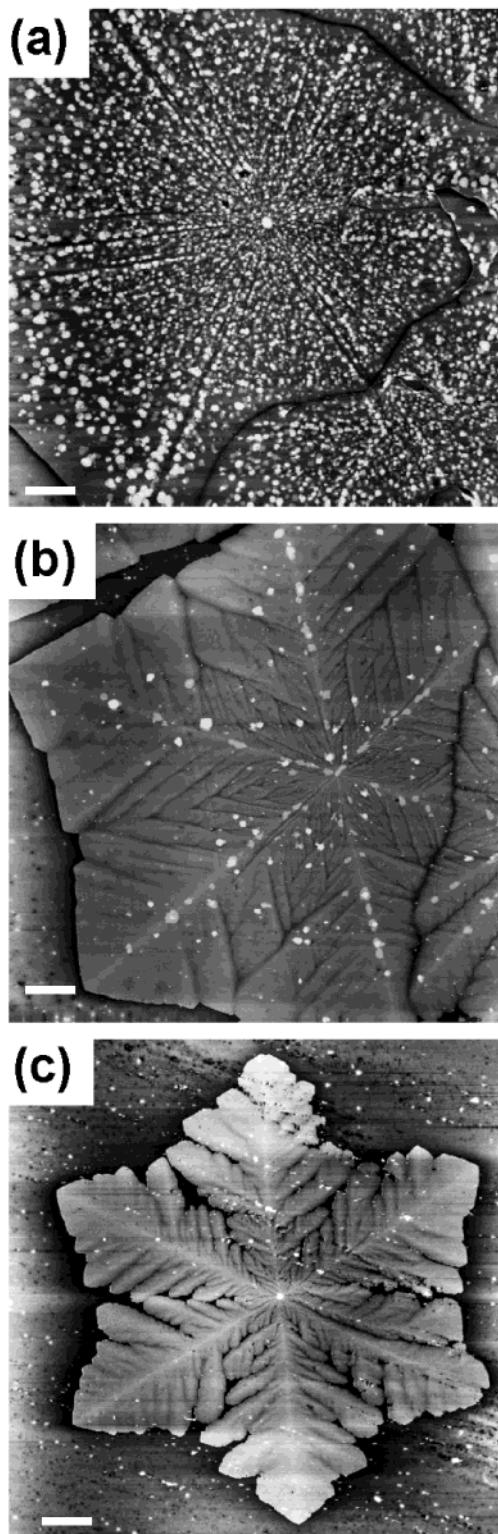


**Figure 7.** AFM height images of ipS crystallized at  $T_x = 193$  °C in a film of gradient thickness  $h$ . (a)  $h = 24$  nm; (b)  $h = 19$  nm; (c)  $h = 15$  nm. The scale bars are 10  $\mu\text{m}$ .

symmetric dendrites in thin ipS films were reported recently, after the present studies were initiated.<sup>13</sup>

In thin polymer films, there is an apparent surface-induced nucleation of crystallization similar to crystallization of polymers onto surfaces from solution. At these values of  $h$ , it is reasonable to consider the films as quasi two-dimensional and thus changes in the crystallization morphology should be expected to arise from spatial confinement. As opposed to the highly disordered patterns

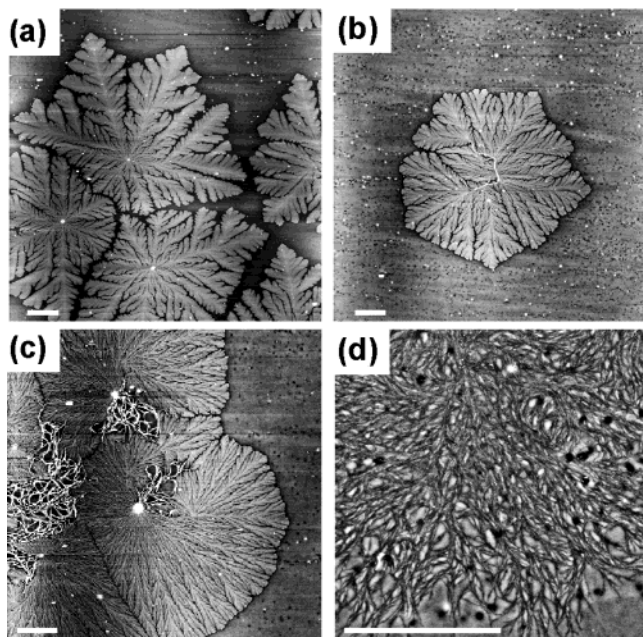


**Figure 8.** AFM height images of hexagonal dendrites, seaweed and "confused" spherulite ipS crystals at  $h < 18$  nm obtained with increased undercooling on a thermal gradient: (a)  $T_x = 169$  °C, (b)  $T_x = 160$  °C, (c)  $T_x = 150$  °C, and (d)  $T_x = 131$  °C. The scale bars are 10  $\mu\text{m}$ . All height scales are 20 nm.

normally found in bulk materials, these thin polymer films can exhibit highly ordered morphologies. Hence, the onset of the influence of secondary nucleation can appear suppressed as the undercooling increases.

Hexagonal and circular crystallization patterns are replaced by hexagonal dendrites (sometimes referred to as dendrites in the polymer literature<sup>38</sup>) and randomly branched dendritic structures, respectively, when  $h < 20$  nm and as the crystallization temperature decreases. Near the same temperature (between 170 and 160 °C and always below  $G_{\text{max}}$ ) at which the 6-fold symmetry of the hexagonal crystal gives way to circular structures, the hexagonal dendrites are replaced by the randomly branched dendritic morphology. These structures are shown in Figure 8, where AFM images captured across the quenched film at different crystallization temperatures in the ultrathin region reveal a progressive loss of symmetry about the nucleation centers. At 150 °C (Figure 8c), the crystalline domain is a combination of disordered network structures composed of threadlike lamellae, forming crystalline superstructures which we consider to be similar to spherulites in thicker films.

When the film is subjected to larger undercooling ( $T_x = 131$  °C, Figure 8d), the slow-growing, networklike

structures grow into large-scale structures with near circular boundaries. The depleted area of the melt then surrounds each crystalline thread rather than the entire spherulite, causing the depressed channels shown in the height image. However, the crystal structures are substantially disordered in comparison to the spherulitic structures obtained at lower undercooling, the resulting crystals resembling splayed crystals found in the early stages of spherulitic growth.<sup>11</sup> These measurements indicate that decreasing film temperature promotes radial growth, consistent with an increased rate of secondary nucleation with higher undercooling and the view that these secondary nucleation processes are the cause of the increasing disorder with increasing undercooling.

## Conclusion

All of the results are consistent with those of conventional, individual experiments and can be efficiently and conveniently obtained based on measurements on two polymer films. (Acquiring the 900 image data sets can be accomplished in less than 2 days, including microscopy measurements.) This high-throughput method of investigating crystallization of semicrystalline polymers in thin films produces information previously requiring numerous films of uniform thickness crystallized at constant temperatures over the duration of the crystallization process. In general, we find excellent agreement with previous laboriously obtained results, validating the high-throughput, combinatorial approach. In the combinatorial experiment, the effects of film thickness and temperature on the growth rate and morphology of ipS were demonstrated across more than 80% of the temperature range in which ipS crystallizes and a full range of film thickness was shown, within which dramatic slowing of rates and morphological transitions occur. No fully developed spherulites or circular crystallization patterns were observed in films having a thickness less than  $R_g$  ( $h < 22$  nm), although structures resembling early-stage spherulitic growth were found at high undercooling. At higher temperatures ( $T_x > 160$  °C), hexagonal dendrites were observed.

The simplicity of the ipS system and similarity of these trends to those found in simulations suggest that molecularly thin ipS films may be an interesting model system for quantitative comparison with developing theory.

**Acknowledgment.** We thank Dr. Cathryn Jackson for early discussions regarding crystallization of ipS in thin films. We also thank Hervé Marand for his helpful feedback on this manuscript. K.L.B. was supported by an NRC/NIST Postdoctoral Fellowship.

**Supporting Information Available:** Figures of the temperature surface map at the air–silicon interface and cross-sectional arrays of the optical image libraries. This material is available free of charge via the Internet at <http://pubs.acs.org>.

LA026751R

(38) Based on personal communication with Hervé Marand.

(39) Equipment and instruments or materials are identified in the paper in order to adequately specify the experimental details. Such identification does not imply recommendation by NIST, nor does it imply the materials are necessarily the best available for the purpose.